Pergamon

Int. J. Solids Structures Vol. 34, No. 26, pp. 3385–3399, 1997

0020–7683/97 $17.00 + .00

PII: S0020–7683(96)00222–3

TAILORING THE PROPERTIES OF PIEZOELECTRIC CERAMICS: ANALYTICAL

S. B. PARK and G. P. CARMAN
Mechanical and Aerospace Eng. Dept., UCLA, Eng IV 38-137m, Los Angeles, CA 90024, U.S.A.

(*Received* 7 *April* 1996; *in revised form* 8 *October* 1996)

Abstract—Piezoelectric ceramics contain anomalies which give rise to localized stress concentrations when electric fields are applied. These stress concentrations cause microcracking which leads to electro-mechanical degradation and eventually to material failure. In this paper, a unit cell approach is presented to understand the relationship between material properties and electric field induced stress concentrations around a specific anomaly, i.e., circular void. An exact electro-elastic analysis verified with a finite element model is used to study the stress and electric field concentrations as a function of material properties. Parametric studies indicate that the electric field induced stress concentrations in the material are effectively eliminated for certain values of the piezoelectric coefficients. While a trivial solution to this problem is that the piezoelectric coefficients are zero, other "optimum" coefficients exist. These coefficients do not limit the deformation profile of the piezoelectric and are thermodynamically admissible. Results presented for PZT-4 and PZT-5H support the contention that optimal piezoelectric materials can be manufactured. © 1997 Elsevier Science Ltd.

1. INTRODUCTION

Among active materials, piezoelectric ceramics (e.g., PZT) are considered to be one of the best actuator materials available. This is partially due to the large actuation forces, large cycle time response, and the relative maturity of research related activities. In fact PZT is currently being used in a number of practical applications such as active optical positioning systems or solid state motors. However, to be implemented in some of the more demanding actuator applications (e.g., active control flap for rotorcraft) these materials must be operated with large electric fields which cause the material to degrade during ferroelectric cycling. The mechanisms which contribute to this degradation process as well as the means to mitigate it need to be more thoroughly investigated.

To analytically understand the degradation process during electric field cycling, researchers focused on fracture toughness. The low fracture toughness of these materials is partially attributable to defects which inevitably form during the sintering process. To evaluate the magnitude of the electric field induced stresses, researchers analytically studied crack geometries as a worst case scenario. However, Parton (1988) reported that the stress fields decouple with electric fields along the self similar plane of the crack. That is, in the plane of the crack electric fields do not induce stress concentrations implying that stress intensity factors commonly used as a fatigue indicator are independent of electric field strength. The total potential energy release rate was proposed by Pak (1990) and later by Suo (1992) as a fracture criteria but the electric fields theoretically retarded crack propagation. These analytical findings which suggest that cracks do not grow in the presence of an electric field are contradicted by experimental evidence (Tobin and Pak (1994)). Dunn (1994) suggested that at least for the slit like crack, the flux boundary conditions along the crack face may influence results and be responsible for reported discrepancies. More recently Park and Sun (1995a, b) proposed the mechanical strain energy release rate as a means to predict the influence of electric fields on crack propagation.

Experimental observations demonstrate that electric fatigue degrades the properties of piezoelectric ceramics (McQuarrie, 1953). Carl (1975) found that micro-cracks form and grow along grain boundaries during fatigue and attributed them to internal stresses. Jiang (1993) reported that electric fatigue is related to the porosity of the ceramic. Pan (1992)

reported that fatigue mechanisms are related to domain pinning issues. Jiang (1994) found that electrode preparation techniques influence electric fatigue behavior. Recently Wang *et al.* (1996) reported that fatigue degradation is caused by stress concentrations around internal anomalies such as voids. While there have been a number of experimental studies on fatigue, these investigations offer different explanations for the fatigue mechanisms with relatively few concentrating on local mechanical stress concentrations. In regards to mechanical loading of piezoceramics, we reference the work of Krueger (1961), Takahashi (1990), and Tanimoto (1991). All of these studies indicate that if the mechanical loads are below the depolarizing stress limit the material does not mechanically degrade. Therefore, mechanical degradation does not appear to be a major concern. In all of these tests whether mechanical or electrical, the influence of the material properties on the fatigue behavior has not been addressed and may offer an explanation to the conflicting data available.

From this brief review, experimental results indicate that piezoelectric materials fatigue in the presence of large electric fields due to the formation of internal damage. Analytical models to describe this behavior are predominantly based on fracture mechanics approaches. In this paper, stress concentrations which arise around cylindrical shaped voids are the principal focus. Unlike the crack, electric fields induce stress concentrations around the symmetric loading plane of a circular hole providing a physical mechanism to induce damage and degrade the material during ferroelectric fatigue. Parametric studies indicate that optimal material properties exist to eliminate the stress states generated by this anomaly which suggests a methodology to alleviate damage progression. While a trivial solution to this condition is that the piezoelectric coefficients are zero, additional optimal properties exist which do not limit the deformation of the material.

2. ANALYTICAL MODELING

Voids or defects present in piezoelectric ceramics may be thought of as randomly distributed spherical shaped cavities (see Fig. 1a). These defects can be analytically modeled as two dimensional hole-like defects (see Fig. 1b) for simplicity. If interaction effects are second order, the problem can be reduced to a single defect as a first order approximation (see Fig. 1c), an approach similar to the analysis of composite materials (Hashin and Rosen, 1964). Physical evidence supporting this modeling approach for a piezoelectric ceramic subjected to ferroelectric fatigue is provided by Wang *et al.* (1996). In Fig. 2a a photograph of a piezoelectric specimen containing a two-dimensional circular defect comparable to the analytical model is presented. During ferroelectric cycling, cracks initiate and grow from the rim of the hole indicating that electric field induced stresses are a primary driving force during fatigue. In Fig. 2b a photograph of a three dimensional micro-void is presented. Similar to the two-dimensional macro-void (Fig. 2a), a crack initiates/grows from the rim of the three-dimensional structure during ferroelectric fatigue. Therefore, the two dimensional unit cell model (Fig. 1c) is thought to be an acceptable approach to begin understanding the relationship between material properties and damage evolution in piezoceramics at the micro-level.

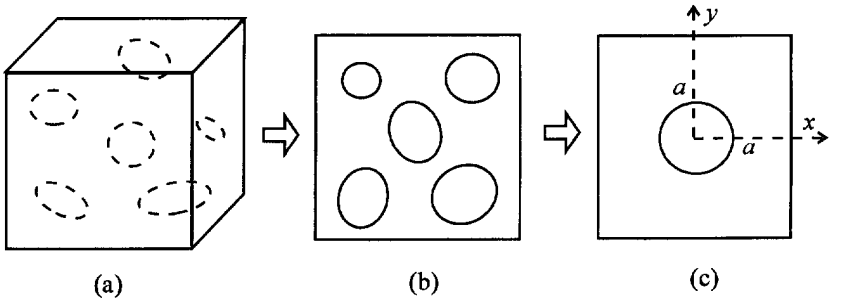

Fig. 1. Modeling of defects, (a) 3-D defects, (b) 2-D defects, (c) unit cell 2-D defect.

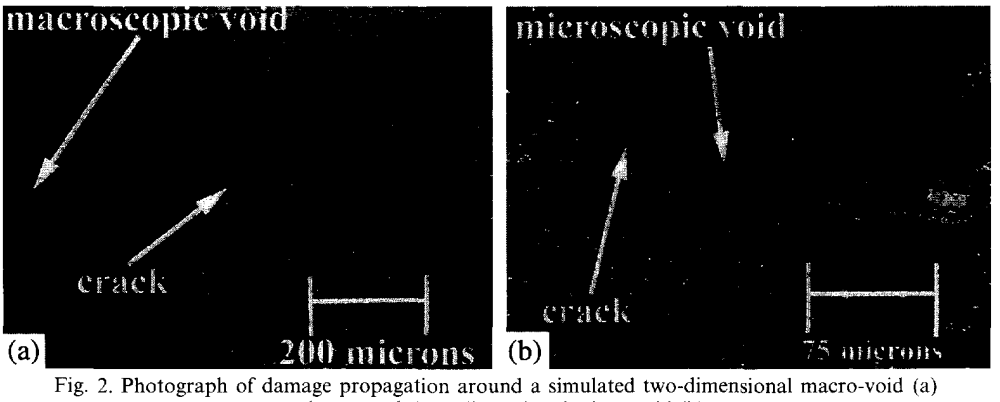

Fig. 2. Photograph of damage propagation around a simulated two-dimensional macro-void (a) and an actual three-dimensional micro-void (b).

Table 1. Material properties of PZT-4 piezoelectric ceramics (Jaffe *et al.*, 1965)

e-form	*g*-form	2-D *g*-form
$c_{11} = 14.02 \times 10^{10}$ (N/m^2)	$s_{11} = 10.90 \times 10^{-12}$ (m^2/N)	$a_{11} = 8.20 \times 10^{-12}$ (m^2/N)
$c_{12} = 7.89 \times 10^{10}$	$s_{12} = -5.42 \times 10^{-12}$	$a_{12} = -3.14 \times 10^{-12}$
$c_{13} = 7.57 \times 10^{10}$	$s_{13} = -2.10 \times 10^{-12}$	$a_{22} = 7.50 \times 10^{-12}$
$c_{33} = 11.58 \times 10^{10}$	$s_{33} = 7.90 \times 10^{-12}$	$a_{33} = 20.88 \times 10^{-12}$
$c_{44} = 2.53 \times 10^{10}$	$s_{44} = 20.88 \times 10^{-12}$	
$e_{31} = -5.27$ (C/m^2)	$g_{31} = -1.11 \times 10^{-2}$ (m^2/C)	$b_{21} = -1.66 \times 10^{-2}$ (m^2/C)
$e_{33} = 15.45$	$e_{33} = 2.61 \times 10^{-2}$	$b_{22} = 2.40 \times 10^{-2}$
$e_{15} = 13.00$	$e_{15} = 3.94 \times 10^{-2}$	$b_{13} = 3.94 \times 10^{-2}$
$\varepsilon_{11} = 6.37 \times 10^{-9}$ (C/Vm)	$\beta_{11} = 8.29 \times 10^{7}$ (Vm/C)	$\delta_{11} = 8.29 \times 10^{7}$ (Vm/C)
$\varepsilon_{33} = 5.52 \times 10^{-9}$	$\beta_{33} = 8.69 \times 10^{7}$	$\delta_{33} = 9.82 \times 10^{7}$

Following Lekhnitskii's (1981) complex potential formulation for anisotropic plates, Sosa (1991) obtained a closed form solution for the problem of a cylindrical cavity embedded in a piezoelectric material. In this section, we briefly summarize the approach and results from the closed form solution. Following this presentation, a finite element model is described for comparison purposes and to validate the exact analytical solution. For this study we use the material properties listed in Table 1 for PZT-4.

2.1. *Analytic solution*

Consider a piezoelectric medium containing a circular hole. Based on linear piezoelectricity, the constitutive relations can be written as

$$S_{ij} = s^{D}_{ijkl}\sigma_{kl} + g_{kij}D_k, \quad E_i = -g_{ikl}\sigma_{kl} + \beta^{\sigma}_{ik}D_k \tag{1}$$

where s^{D}_{ijkl} is the compliance tensor measured at constant electric displacement, g_{kij} is the piezoelectric stress tensor, and β^{σ}_{ij} is the dielectric impermeability tensor measured at constant stress. Although there are several different types of expression for the constitutive relations, the expression in eqn (1), called *g*-form, which has stresses, σ_{kl}, and electric displacements, D_k, as independent variables was chosen to facilitate the development of complex stress potentials. The relation between material coefficients for other forms of constitutive relations can be easily derived by changing independent variables.

Equilibrium equations are written as

$$\sigma_{ij,j} = 0, \quad D_{i,i} = 0. \tag{2}$$

Generally, the x_3 axis represents the poling direction of the material in axes, $x_1 - x_2 - x_3$. Most piezoelectric ceramics have a tetragonal structure and are transversely isotropic with the x_3 axis normal to the isotropic plane. For our problem, the $x_1 - x_3$ plane is the working plane and it will be denoted as the x-y plane. By reducing the problem to 2-D plane strain case, the following conditions are imposed.

$$S_{22} = S_{32} = S_{12} = E_2 = 0. \tag{3}$$

Using the conditions imposed by eqn (3) in eqn (1), the constitutive relations can be reduced to two-dimensions in the following matrix form.

$$\begin{Bmatrix} S_{xx} \\ S_{yy} \\ S_{xy} \end{Bmatrix} = \begin{bmatrix} a_{11} & a_{12} & 0 \\ a_{12} & a_{22} & 0 \\ 0 & 0 & a_{33} \end{bmatrix} \begin{Bmatrix} \sigma_{xx} \\ \sigma_{yy} \\ \sigma_{xy} \end{Bmatrix} + \begin{bmatrix} 0 & b_{21} \\ 0 & b_{22} \\ b_{13} & 0 \end{bmatrix} \begin{Bmatrix} D_x \\ D_y \end{Bmatrix} \tag{4}$$

$$\begin{Bmatrix} E_x \\ E_y \end{Bmatrix} = -\begin{bmatrix} 0 & 0 & b_{13} \\ b_{21} & b_{22} & 0 \end{bmatrix} \begin{Bmatrix} \sigma_{xx} \\ \sigma_{yy} \\ \sigma_{xy} \end{Bmatrix} + \begin{bmatrix} \delta_{11} & 0 \\ 0 & \delta_{22} \end{bmatrix} \begin{Bmatrix} D_x \\ D_y \end{Bmatrix}. \tag{5}$$

The constants of a_{ij}, b_{ij}, and δ_{ij} are listed in Table 1. To solve the problem using a complex potential approach the compatibility equations are required.

$$\frac{\partial^2 S_{xx}}{\partial y^2} + \frac{\partial^2 S_{yy}}{\partial x^2} - 2\frac{\partial^2 S_{xy}}{\partial x\,\partial y} = 0, \quad \frac{\partial E_x}{\partial y} - \frac{\partial E_y}{\partial x} = 0. \tag{6}$$

Stress functions and electric displacement functions which satisfy field equations, eqns (2)–(6), can be defined as

$$\sigma_{xx} = \frac{\partial^2 U}{\partial y^2}, \quad \sigma_{yy} = \frac{\partial^2 U}{\partial x^2}, \quad \sigma_{xy} = -\frac{\partial^2 U}{\partial x\,\partial y}, \quad D_x = \frac{\partial \psi}{\partial y}, \quad \text{and} \quad D_y = -\frac{\partial \psi}{\partial x} \tag{7}$$

where U and ψ are functions of a complex variable, z, defined as $z = x + \mu y$. Applying stress and electric displacement functions, eqn (7), to compatibility equations, eqn (6), a characteristic equation can be obtained. Once the roots of the characteristic equation, $\mu_k = \alpha_k + i\beta_k$, are known, the solution can be expressed as

$$U(x, y) = 2\,\mathrm{Re} \sum_{k=1}^{3} U_k(z_k) \tag{8}$$

where $z_k = x + \mu_k y$. From either one of the two compatibility equations, the relation between U and ψ can be obtained as follows.

$$\psi_k(z_k) = \lambda_k U_k'(z_k) \tag{9}$$

where

$$\lambda_k = -\frac{(b_{21} + b_{13})\mu_k^2 + b_{22}}{\delta_{11}\mu_k^2 + \delta_{22}}. \tag{10}$$

Hence, the solution for the electric displacement function can be written

$$\psi(x, y) = 2\,\mathrm{Re} \sum_{k=1}^{3} \psi_k(z_k) = 2\,\mathrm{Re} \sum_{k=1}^{3} \lambda_k U_k'(z_k). \tag{11}$$

To reduce the order of the derivative, we introduce a complex variable φ_k as $\varphi_k(z_k) = U_k'$. The stresses and electric displacements can then be expressed as a function of φ_k.

$$\sigma_{xx} = 2\,\mathrm{Re} \sum_{k=1}^{3} \mu_k^2 \varphi_k'(z_k), \quad \sigma_{yy} = 2\,\mathrm{Re} \sum_{k=1}^{3} \varphi_k'(z_k), \quad \sigma_{xy} = -2\,\mathrm{Re} \sum_{k=1}^{3} \mu_k \varphi_k'(z_k)$$

$$D_x = 2\,\mathrm{Re} \sum_{k=1}^{3} \lambda_k \mu_k \varphi_k'(z_k), \quad D_y = -2\,\mathrm{Re} \sum_{k=1}^{3} \lambda_k \varphi_k'(z_k). \tag{12}$$

Now the problem is reduced to determining a complex function φ satisfying boundary conditions. Two types of boundary conditions are applied. One is the remote mechanical and electrical loading, and the other is the hole boundary conditions. As was shown in Fig. 1, the hole has radius a. Far field remote loadings can be denoted as

$$\sigma_{xx}^{\infty} = 0, \quad \sigma_{xy}^{\infty} = 0, \quad \sigma_{yy}^{\infty} = 0, \quad D_x^{\infty} = 0, \quad \text{and} \quad D_y^{\infty} = D_0 \quad \text{at } z = \infty. \tag{13}$$

The rim of the hole is traction free and to a first order approximation it can be argued that the hole is electrically insulated. The validation of the latter boundary condition is justified by the fact that the dielectric permittivity of piezoelectric ceramics is three orders of magnitude larger than air or vacuum. Here, boundary condition along the rim of hole, Γ, can be written as

$$t_i = 0 \quad \text{and} \quad D_i n_i = 0 \quad \text{on } \Gamma \tag{14}$$

where t_i is the traction vector and n_i is the unit normal vector to the circular hole of contour Γ.

Applying the hole boundary conditions (eqn (14)) and the far-field boundary conditions (eqn (13)) the complex potential function can be obtained as

$$\varphi_k(z_k) = (B_k + iB_k^*)z_k + \Lambda_k D_0 \frac{z_k - \sqrt{z_k^2 - a^2(1+\mu_k^2)}}{2(1+i\mu_k)} \tag{15}$$

where

$$\Lambda = \frac{1}{\Delta}\begin{bmatrix} \mu_3 - \mu_2 \\ \mu_1 - \mu_3 \\ \mu_2 - \mu_1 \end{bmatrix}$$

and

$$\Delta = (\lambda_2 - \lambda_3)\mu_1 + (\lambda_3 - \lambda_1)\mu_2 + (\lambda_1 - \lambda_2)\mu_3$$

where B_k and B_k^* are real constants determined by the boundary conditions (eqn (13)). Substituting eqn (15) into eqn (12), full field solutions such as stresses and electric displacements can be obtained.

2.2. *Finite element analysis*

In addition to the analytical model, a finite element analysis (FEA) was performed to check the validity of the analytic solution. Commercially available FEA packages such as ANSYS and ABAQUS, as well as an in-house code were used for comparison purposes. All three codes yielded displacements and potential values differing by less than 2%. In Fig. 3 we present an illustration of the finite element model used in this study. Considering

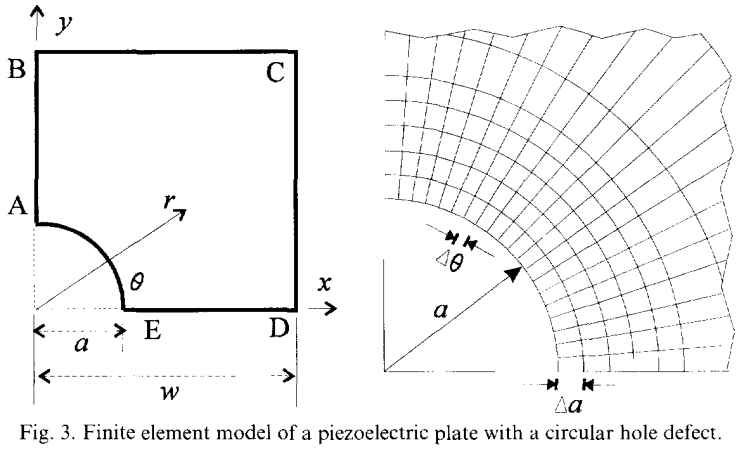

Fig. 3. Finite element model of a piezoelectric plate with a circular hole defect.

symmetry, one quarter of the plate was analyzed. Results presented in this manuscript correspond to a radius to width ratio, a/w of 0.1 to simulate an infinite plate with a hole. For mechanical problems, if the a/w ratio is less than 0.25 the error in calculating hoop stresses is less than 6% (Timoshenko, 1934). The size of the elements near the hole was $\Delta a/a = 0.01$ and $\Delta\theta = 4.5$ degrees (see Fig. 3b). Mesh refinement to $\Delta a/a = 0.005$ with 40 elements along the hoop direction were conducted without appreciable changes in the primary variables.

Four noded piezoelectric quadratic plane strain elements were used with each node having three degrees of freedom (DOF), i.e., two displacements, u and v, and an electric potential, ϕ. Mechanical boundary conditions are imposed along lines AB and ED with x displacements constrained and y displacements constrained, respectively. For the electric boundary conditions, electric potentials were imposed along the lines BC and ED. Since the electric boundary conditions in the analytic model are electric displacement D_0 (eqn (14)) and not electric potential as in the finite element model, an equivalence principal was used. This was calculated with the constitutive equations, eqn (1), which related the far-field electric field to the far-field electric displacement for an equivalent medium.

In developing the finite element analysis, the constitutive relations presented in eqns (16–17) were used. That is, strains and electric fields were used as the free variables, i.e., e-form, as opposed to electric displacements and stresses (compare to eqn (1)). Results presented in this paper are also described in the context of e-form due to its wider acceptance. The material constants used in all of the analysis are representative of PZT-4 listed in Table 1.

$$\begin{Bmatrix}\sigma_{xx}\\ \sigma_{yy}\\ \sigma_{xy}\end{Bmatrix} = \begin{bmatrix}c_{11} & c_{13} & 0\\ c_{13} & c_{33} & 0\\ 0 & 0 & c_{44}\end{bmatrix}\begin{Bmatrix}S_{xx}\\ S_{yy}\\ S_{xy}\end{Bmatrix} + \begin{bmatrix}0 & e_{31}\\ 0 & e_{33}\\ e_{15} & 0\end{bmatrix}\begin{Bmatrix}E_x\\ E_y\end{Bmatrix} \tag{16}$$

$$\begin{Bmatrix}D_x\\ D_y\end{Bmatrix} = \begin{bmatrix}0 & 0 & e_{15}\\ e_{31} & e_{33} & 0\end{bmatrix}\begin{Bmatrix}S_{xx}\\ S_{yy}\\ S_{xy}\end{Bmatrix} + \begin{bmatrix}\varepsilon_{11} & 0\\ 0 & \varepsilon_{33}\end{bmatrix}\begin{Bmatrix}E_x\\ E_y\end{Bmatrix}. \tag{17}$$

3. RESULTS

The electric flux is applied in the negative y-direction for all cases studied in this paper. The far field electric field is defined by $-E_0$ and unless otherwise specified the results pertain to the analytical solution presented in Section 2.1. In Fig. 4, we compare numerical results obtained from the analytical solution to that of the finite element model for PZT-4. The normalized hoop stress along the rim of the hole is plotted as a function of azimuth angle.

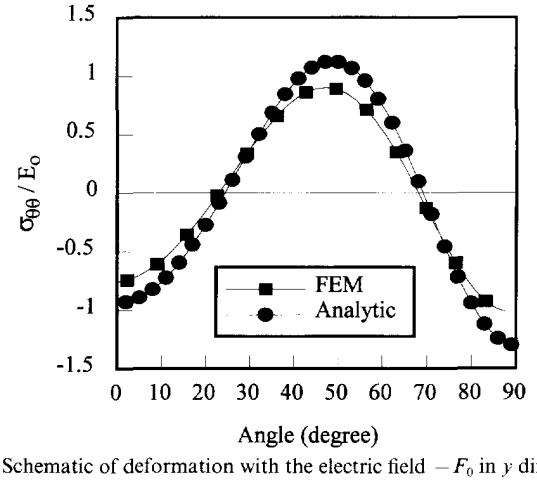

Fig. 4. Schematic of deformation with the electric field $-F_0$ in y direction.

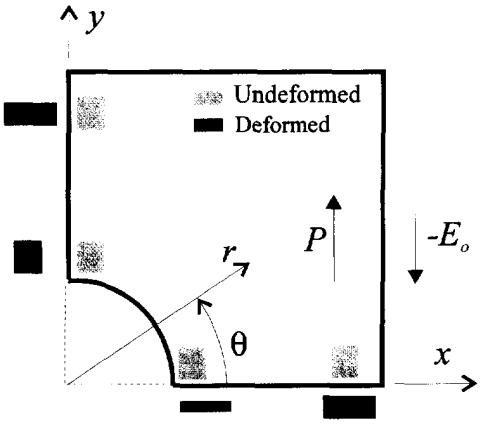

Fig. 5. Physical explanation of electric field induced stresses in the piezoceramic due to a $-E_y$.

The hoop stress in the figure is normalized to the far field electric field value ($-E_0$). Comparison between the two models indicates reasonable agreement indicating that both solutions are valid. Differences between the models can be attributed to both mesh size and evaluation of the hoop stresses at particular points. For the analytical solution the hoop stresses are calculated along the rim of the hole while for the FEA analysis they are calculated at the Gauss points for the element. For either model the hoop stress is compressive at both $\theta = 0°$ and 90° while tensile at $\theta = 45°$. A physical explanation based on an electric field directed in the y-direction (E_y) suggests that these stresses should be tensile (see Fig. 5) and not compressive. That is, an element at the rim of the hole at $\theta = 0°$ will experience a relatively larger contraction than a similar element in the far field at $\theta = 0°$ resulting in a tensile hoop stress. Also at $\theta = 90°$, the electric field vanishes in the y-direction due to the imposed flux condition (eqn (15)) suggesting that this element should also be in tension. Therefore, an explanation based solely on E_y is insufficient to explain the compressive stress concentrations present in PZT-4.

To investigate other mechanisms generating stress concentrations within the material, the normalized electric field variations (both x and y) around the rim of the hole are presented in Fig. 6. The normalized y-directed electric field strength E_y/E_0 increases by a factor of 2 at $\theta = 0°$ while at 90° it nearly vanishes as expected. The E_y is associated with the longitudinal piezoelectric coefficients (e_{31} and e_{33}) causing the physical deformations/stresses depicted in Fig. 5 and discussed in the previous paragraph. Figure 6 also indicates the presence of a x-directed electric field (E_x) around the rim of the hole and at certain locations is comparable in magnitude to the E_y. The E_x generates additional stresses which are

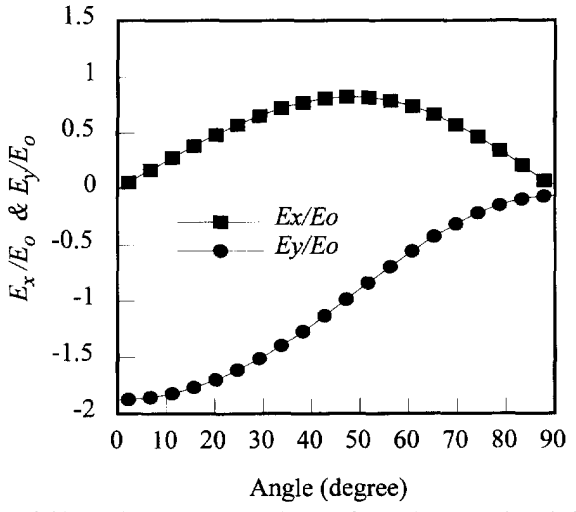

Fig. 6. Electric field distribution normalized to far-field value around the hole $r/a = 1.0$.

associated with the piezoelectric shear coefficient (i.e., e_{15}) and was not previously considered. To quantitatively evaluate the stress fields generated by E_x and E_y, an analytical study of two hypothetical piezoelectric materials is presented. The first material has a piezoelectric shear coefficient e_{15} equal to zero and all other reflective of PZT-4. For this material, the E_x does not induce any stresses/strains while E_y does. For the second material, the piezoelectric longitudinal stress coefficients e_{31} and e_{33} are identically zero while e_{15} is representative of PZT-4. For this material only E_x induces stresses/strains into the specimen. By evaluating these two cases, the contribution of E_x or E_y fields to the hoop stress can be determined by modulating e_{15} or e_{31} and e_{33}.

In Fig. 7, the normalized hoop stress is plotted as a function of azimuth angle at $r/a = 1$ for the two hypothetical materials. An E_x electric field (related to shear coefficient term (e_{15})) generates stresses opposite in sign to the E_y (related to longitudinal coefficient terms (e_{31} and e_{33})). For the hypothetical material with the shear coefficient, compressive hoop stresses are generated at both $\theta = 0^\circ$ and 90°, while for the other material tensile hoop stresses are generated at these locations. While these two effects cannot be simply superimposed for determining absolute magnitudes due to coupling in the partial differential equations (i.e., plug eqns (16) and (17) into eqn (2)), this analysis provides an indication of their influence on stress distributions. Specifically, for PZT-4 the presence of compressive stresses at either $\theta = 0^\circ$ or 90° is attributed to the relative magnitude of the piezoelectric shear coefficients when compared to the piezoelectric longitudinal coefficients. While this study provides both a physical and a mathematical explanation for the compressive hoop stresses generated in PZT-4, the results presented in Fig. 7 have a significantly more important meaning. They suggest that by appropriately choosing the material properties (e_{15}, e_{31}, and e_{33}) the hoop stress around the rim of the hole can be reduced/eliminated.

To elaborate upon this concept, Fig. 8 displays the results of a parametric study demonstrating that the hoop stress can be reduced. This study includes coupling in the partial differential equations and therefore is an accurate depiction, unlike Fig. 7 which was presented only for clarification of a physical idea. The normalized hoop stress distribution is plotted as function of θ at the hole's rim for different e_{15}. In the study only e_{15} was varied while all other material constants were fixed. As e_{15} decreases in absolute magnitude from the original value, $e_{15} = 13.0$ C/m^2, the hoop stress begins to decrease in magnitude. At a value of $e_{15} = 11.0$ C/m^2, the hoop stress around the rim is almost entirely eliminated. Further decreases in e_{15} cause the hoop stress to reverse suggesting that the longitudinal piezoelectric coefficients have become sufficiently large to dominate the problem. For all materials studied in this graph, nodal points indicating an absence of stress arise at 22° and 68° and local minimums/maximums occur at 0°, 45°, and 90°. The presence of these fixed

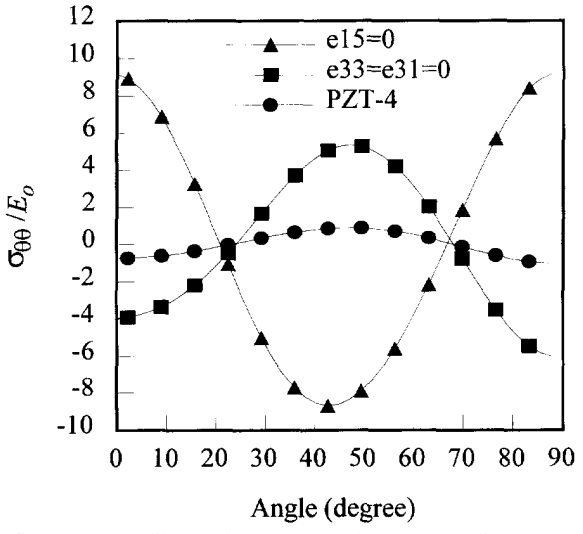

Fig. 7. Hoop stress distribution at $r/a = 1.0$ for hypothetical materials.

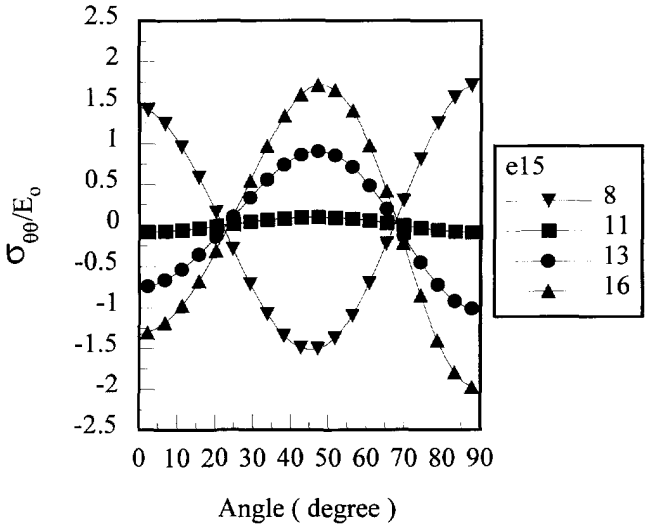

Fig. 8. Hoop stress distribution at $r/a = 1.0$ for different values of e_{15}.

points strongly suggests that the hoop stress can be entirely eliminated with an appropriate choice of the shear coefficient.

Similar parametric studies using e_{31} and e_{33} are presented in Figs 9 and 10, respectively. While e_{15} is an independent material parameter, some experimental results have indicated that a relationship exists between e_{31} and e_{33} based on a constant volume argument (Jaffe, 1971). While this suggests that these two parameters cannot be independently varied, the proposed parameters presented in Figs 8–10 represent reasonable variations of the constants. In Fig. 9, the value of e_{31} is varied from -5.3 to -14 C/m^2 with results similar to those presented in Fig. 8 for e_{15}. However, for a value of $e_{31} = -9.6$ C/m^2 the entire hoop stress around the rim of the hole appears to be eliminated. This provides conclusive evidence that the piezoelectric coefficients can be modified to control and eliminate the hoop stresses around the rim of the hole. Furthermore, for this optimal case the deformation of the piezoelectric medium is larger than for the original coefficients. Therefore, optimum piezoelectric properties do not limit deformations. When reviewing Figs 9 and 10, nodal points are present at 22° and 68° as well as maximum and minimums arising at 0°, 45°, and 90°. This indicates that the stress states vary in a specific fashion for all variations in the piezoelectric coefficient implying that optimal coefficients can be calculated by demanding that the hoop stress vanish at any non-zero location around the rim.

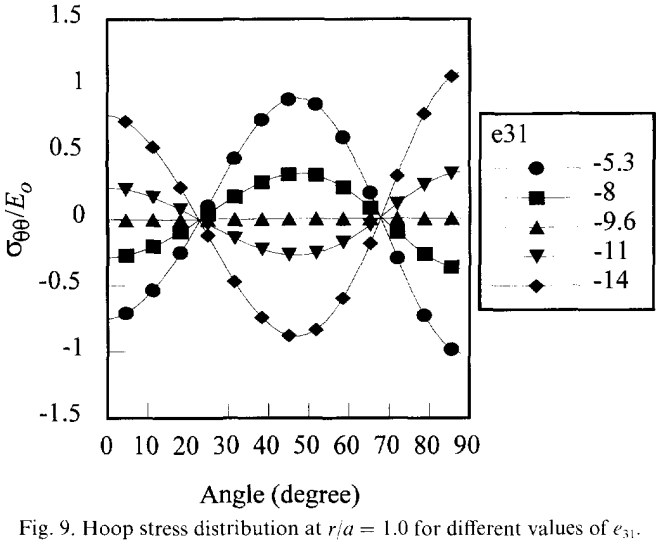

Fig. 9. Hoop stress distribution at $r/a = 1.0$ for different values of e_{31}.

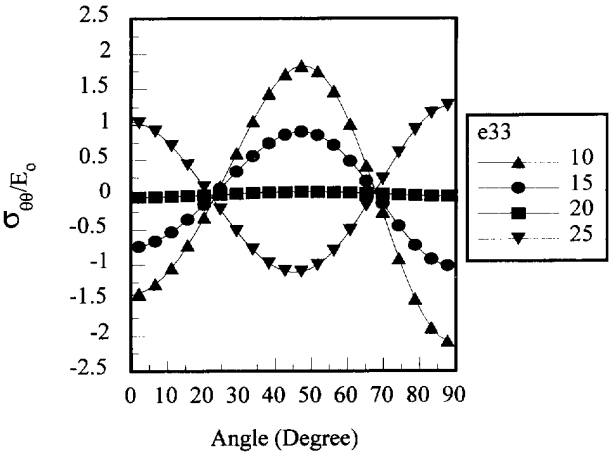

Fig. 10. Hoop stress distribution at $r/a = 1.0$ for different values of e_{33}.

In Figs 8–10 parametric studies were presented to evaluate the variation in hoop stress as a function of specific material properties. These results demonstrated that optimum properties exist and could be calculated by eliminating the stress at any non-zero location. To more accurately predict the optimal piezoelectric coefficients, Fig. 11 displays the variation in hoop stress as a function of material properties. In this figure, each piezoelectric coefficient is varied over a wide range of values while the other ones are held constant. Only the hoop stress at $\theta = 0$ is presented in this figure with magnitudes at other locations along the rim being qualitatively inferred from the results presented in Figs 8–10. That is, the trend in the hoop stress variation remains fixed, such that nodal points occur at 22° and 68° and maximum/minimums at 0°, 45°, and 90°. As a result the values which cause the hoop stress to vanish in Fig. 11 represent an optimal configuration for the piezoelectric coefficients. The optimal values of e_{33}, e_{15}, and e_{31} are 20.15, 10.75, and -9.63 (C/m^2), respectively. Any one of these values effectively eliminates the hoop stress around the rim of the hole. These results are more accurate estimates than the values presented in Figs 8–10. While this result demonstrates that hoop stresses around the rim are eliminated, the entire stress state in the material is also essentially eliminated. Support for this statement is provided by the fact that stresses arise because of stress generators. If there does not exist any stress generators in the material it will be stress free. The fact that the far-field stresses are identically zero (eqns (13)–(16)) and both the tractions and hoop stresses are essentially zero around the rim of the hole indicates the absence of stress generators in the medium.

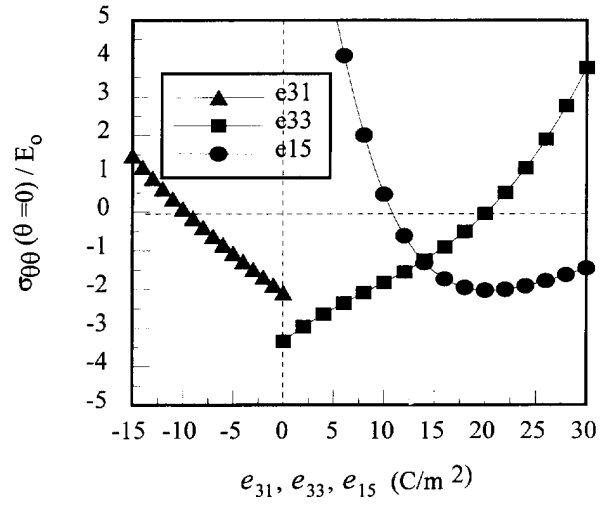

Fig. 11. Hoop stress at $\theta = 0$ and $r/a = 1.0$ with piezoelectric constants, e_{ij}, as parameters.

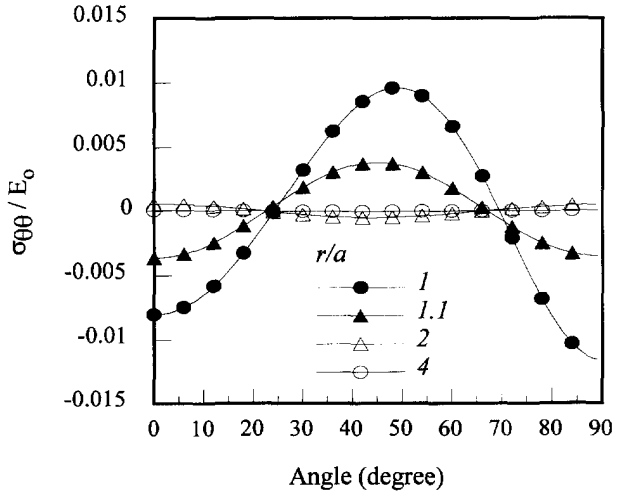

Fig. 12. Hoop stress distribution at different radial positions for $e_{31} = -9.6$ C/m^2.

To verify this, Fig. 12 presents the variations in the normalized hoop stress at different radial positions for $e_{31} = -9.6$ C/m^2. The results indicate that the hoop stress is essentially eliminated everywhere in the material. While the e_{31} value chosen for this study is not the exact optimum, the stresses are two orders of magnitude smaller than they are for PZT-4 (see Fig. 4). In Fig. 12, the largest hoop stress occurs along the rim of the hole ($r/a = 1$) and quickly decays as the radial position is increased. This exponential like decay contributes to the discrepancies between the finite element calculated hoop stresses and the analytical result reported in Fig. 4, that is the finite element stresses are calculated at Gauss points.

Figure 13 is provided to further support the contention that the entire stress state is eliminated in the medium. The normalized hoop, radial, and shear stress variation at $r/a = 1.1$ is presented for PZT-4 with $e_{31} = -9.63$ C/m^2. This value is closer to the optimum value than the one used to generate Fig. 12. The hoop stress for this particular material is four orders of magnitude smaller than the hoop stress for PZT-4 in Fig. 4 and two orders of magnitude smaller than the hoop stress presented in Fig. 12. While the stresses are not identically zero for $e_{31} = -9.63$ C/m^2 (i.e., 10^{-4}) for all practical purposes they are. The fact that they are not zero indicates that additional terms must be kept to completely zero out the stress state. These results clearly indicate that optimal properties predicted by the present analysis eliminates the entire stress field in a piezoceramic containing a void.

In Fig. 14, the hoop stresses at the rim of a hole for two commercially available materials is presented, i.e., PZT-5H and PZT-4. The material properties for PZT-5H are published by Channel Industries a manufacturer of both material systems. For PZT-5H,

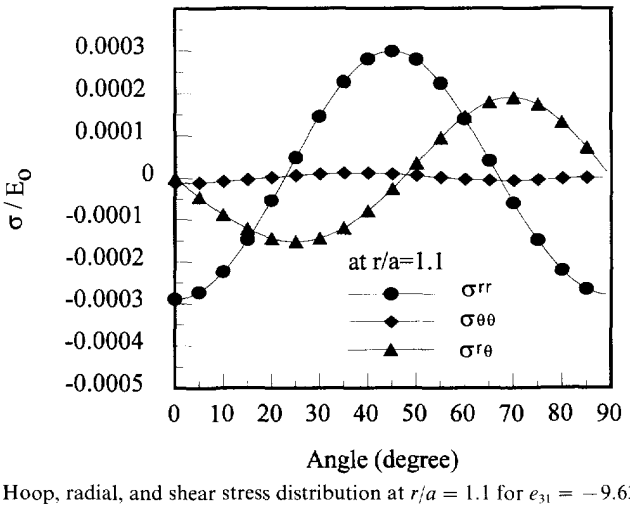

Fig. 13. Hoop, radial, and shear stress distribution at $r/a = 1.1$ for $e_{31} = -9.63$ C/m^2.

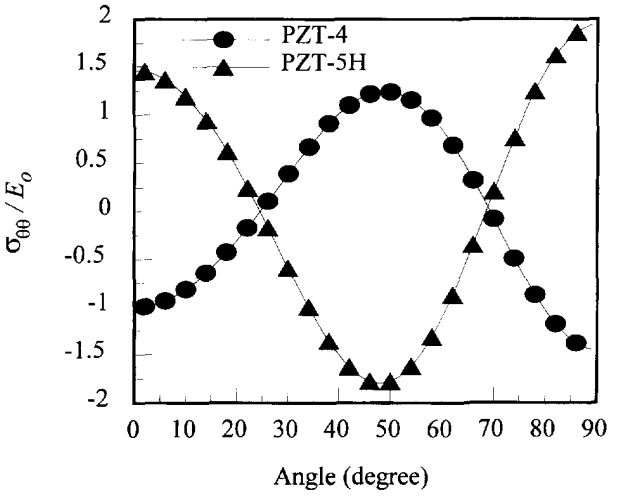

Fig. 14. Comparison of hoop stress distribution at $r/a = 1.0$ for PZT-4 and PZT-5H.

the stresses around the periphery of the hole are opposite in sign to the stresses for PZT-4. Specifically, at $\theta = 0^\circ$ and 90° the hoop stresses are tensile which is in sharp contrast to the compressive stresses for PZT-4. This indicates that for PZT-5H the stresses are dominated by the longitudinal piezoelectric coefficients and not the shear piezoelectric coefficient as they are for PZT-4 (see Fig. 7 and related discussion). While opposite in sign, both materials undergo stress reversal during bipolar electric cycling which could lead to fatigue degradation. While neither of these materials represents an optimum, the fact that the inherent stress fields are controlled by different piezoelectric coefficients indicates the plausibility of developing a material with optimal properties predicted by the analysis presented in this manuscript.

4. CONCLUSION

In this paper we discovered that the piezoelectric coefficients could be tailored to eliminate the electric field induced stresses in a medium containing a circular defect. A trivial solution to this problem is that the piezoelectric coefficients are all zero. However, additional solutions exist and these other solutions permit large deformation of the piezoceramic material. The stress concentrations around a circular hole were shown to be attributable to either the shear or the normal piezoelectric coefficients. By choosing specific values of these coefficients we demonstrated that the stress concentrations around the hole and in the entire medium could be eliminated. This suggested that the fatigue life of these materials could be increased through appropriate modification during the manufacturing process. The proposed coefficients are thermodynamically admissible and do not limit the deformation profile of the ceramic.

Acknowledgment—This research work was supported by the Army Research Office under contract DAAH04-95-1-0095. Technical monitor is Dr John Prater.

REFERENCES

Carl, K. (1975). Ferroelectric properties and fatiguing effects of modified $PbTiO_3$ ceramics. *Ferroelectrics* **9**, 23–32.

Dunn, M. (1994). The effects of crack face boundary conditions on the fracture mechanics of piezoelectric solids. *Engineering Fracture Mechanics* **48**, 25–39.

Hashin, Z. and Rosen, R. W. (1964). The fracture modeling of fiber-reinforced materials. *Journal of Applied Mechanics* **31**, 223–232.

Ikeda, T. (1990). *Fundamentals of Piezoelectricity*. Oxford Science Publications, Oxford, U.K.

Jaffe, H. and Berlincourt, D. A. (1965). Piezoelectric transducer materials. *Proceedings of the IEEE* **53**(10), 1372–1386.

Jaffe, B. and Cook, W. (1971). *Piezoelectric Ceramics*. Academic Press.

Jiang, Q. and Cross, L. E. (1993). Effects of porosity on electric fatigue behavior in PLZT and PZT ferroelectric ceramics. *Journal of Material Science* **28,** 4536–4543.

Jiang, Q. Y., Cao, W. and Cross, L. E. (1994). Electric fatigue in lead zirconate titanate ceramics. *Journal of American Ceramic Society* **77,** 211–215.

Krueger, H. H. A. and Berlincourt, D. (1961). Effects of high static stress on the piezoelectric properties of transducer materials. *Journal of the Acoustical Society of America* **33,** 1339–1344.

Lekhnitskii, S. G. (1981). *Theory of Elasticity of an Anisotropic Body*, Mir Publishers, Moscow.

McQuarie, M. (1953). Time effects in the hystersis loop of polycrystalline barium titanate. *Journal of Applied Physics* **24,** 1334–1335.

Pak, Y. E. (1990). Crack extension force in a piezoelectric material. *Journal of Applied Mechanics* **57,** 647–653.

Pan, W., Yue, C.-F. and Sun, S. (1992). Domain orientation change induced by ferroelectric fatigue process in lead zirconate titanate ceramics. *Ferroelectrics* **133,** 97–102.

Park, S. B. and Sun, C. T. (1995a). Effect of electric field on fracture of piezoelectric ceramics. *International Journal of Fracture* **70,** 203–216.

Park, S. B. and Sun, C. T. (1995b). Fracture criteria for piezoelectric ceramics. *Journal of American Ceramic Society* **78,** 1475–1480.

Park, S. B. and Carman, G. P. (1996). Minimizing stress concentration in piezoelectric media containing ellipsoidal voids. *Journal of Applied Mechanics* (in press).

Parton, V. Z. and Kudryavtsev, B. A. (1988). *Electromagnetoelasticity*. Gordon and Breach Science Publishers, New York.

Sosa, H. A. (1991). Plane problems in piezoelectric media with defects. *International Journal of Solids and Structures* **28,** 491–505.

Suo, Z., Kuo, C.-M., Barnett, D. M. and Willis, J. R. (1992). Fracture mechanics for piezoelectric ceramics. *Journal of Mechanics and Physics of Solids* **40**(4), 739–765.

Takhashi, S., Okajima, K. and Hasegawa, A. (1990). Fatigue degradation and reliability of piezoelectric ceramics. *Japanese Journal of Applied Physics* **29,** 47–49.

Tanimoto, T. and Okazaki, K. (1991). Fatigue test of piezoelectric ceramics under high hydrostatic pressure. *Japanese Journal of Applied Physics* **30,** 2410–2412.

Tobin, A. G. and Pak, Y. E. (1993). Effect of electric fields on fracture behavior of PZT ceramics. *Proceedings of SPIE, Smart Structures and Materials* **1916,** 78–86.

Wang, D., Carman, G. P. and Fotinich, Y. (1996). Influence of temperature on the electro-mechanical and fatigue behavior of piezoelectric ceramics. *Journal of Applied Physics* (in press).